Frontiers of Information Technology & Electronic Engineering
www.zju.edu.cn/jzus; engineering.cae.cn; www.springerlink.com
ISSN 2095-9184 (print); ISSN 2095-9230 (online)
E-mail: jzus@zju.edu.cn

Effects of residual motion compensation errors on the performance of airborne along-track interferometric SAR*

Hui ZHANG†[1,2,3], Jun HONG[1], Xiao-lan QIU[1,3], Ji-chuan LI[4], Fang-fang LI[1,3], Feng MING[1]

([1]*Institute of Electronics, Chinese Academy of Sciences, Beijing 100190, China*)

([2]*University of the Chinese Academy of Sciences, Beijing 100190, China*)

([3]*Key Laboratory of Technology in Geo-spatial Information Processing and Application Systems, Beijing 100190, China*)

([4]*Science and Technology on Millimeter-Wave Laboratory, Beijing 100854, China*)

†E-mail: 123happy.zh@163.com

Received Sept. 25, 2015; Revision accepted Feb. 18, 2016; Crosschecked Sept. 12, 2016

Abstract: Two approximations, center-beam approximation and reference digital elevation model (DEM) approximation, are used in synthetic aperture radar (SAR) motion compensation procedures. They usually introduce residual motion compensation errors for airborne single-antenna SAR imaging and SAR interferometry. In this paper, we investigate the effects of residual uncompensated motion errors, which are caused by the above two approximations, on the performance of airborne along-track interferometric SAR (ATI-SAR). The residual uncompensated errors caused by center-beam approximation in the absence and in the presence of elevation errors are derived, respectively. Airborne simulation parameters are used to verify the correctness of the analysis and to show the impacts of residual uncompensated errors on the interferometric phase errors for ATI-SAR. It is shown that the interferometric phase errors caused by the center-beam approximation with an accurate DEM could be neglected, while the interferometric phase errors caused by the center-beam approximation with an inaccurate DEM cannot be neglected when the elevation errors exceed a threshold. This research provides theoretical bases for the error source analysis and signal processing of airborne ATI-SAR.

Key words: Synthetic aperture radar (SAR), Along-track interferometric, Motion compensation, Residual error, Interferometric phase

http://dx.doi.org/10.1631/FITEE.1500311 **CLC number:** TN959.73

1 Introduction

Along-track interferometric synthetic aperture radar (ATI-SAR), which uses the interferometric SAR (InSAR) technique, can be used to map ocean current velocities, and was reported for the first time by Goldstein and Zebker (1987). The ATI-SAR technique is also applied for detecting slowly moving targets, such as ground moving target indication (GMTI) (Glerull, 2002; Imel, 2002; Chen, 2004; Zhang, 2006; Budillon *et al.*, 2008; Chapin and Chen, 2009). The widely used cross-track InSAR (XTI-SAR) techniques (Rosen *et al.*, 2000; Zink *et al.*, 2007) map digital elevation models (DEMs) by using dual-channel (or multi-channel) SAR data acquired with antenna phase centers separated in the direction perpendicular to the flight direction. In contrast, ATI-SAR techniques use two or more antenna phase centers, which are physically separated along the platform flight path to acquire interferometric SAR data. Each ATI antenna illuminates the same scene at the same position with a fixed time interval during which the platform travels the along-track offset between the two-phase centers. Therefore, while the stationary elements of the imaged scene remain unchanged and contribute identically to the images, the

* Project supported by the National Natural Science Foundation of China (Nos. 61331017 and 61401428)

ORCID: Hui ZHANG, http://orcid.org/0000-0002-4304-0411

moving targets in the scene move to different positions after the time interval and the antenna-target ranges change between different SAR images. By interferometrically processing the complex SAR images acquired by different ATI antennas, the interferometric phase, which relates to the radial velocities of the moving targets, can be obtained.

Motion compensation is a key step in airborne SAR imaging procedures. In the ideal case, the platform equipped with radar antennas moves with constant velocity and constant height along a linear trajectory. However, in a real flight, especially for the airborne platform ones, the aircraft's position will change due to the atmospheric perturbation and strong winds. Thus, the trajectory of the airplane will deviate from the nominal one, and the forward velocity will no longer be a constant. If not properly accounted for during the processing, this deviation will introduce motion errors on the received SAR data and may strongly impair the final image quality, including the loss of geometric and radiometric resolution (Raney, 1971; Fornaro *et al.*, 2005) and absolute phase errors. Usually the Inertial Navigation Units (INU) and Global Positioning System (GPS) are mounted on-board the airplane to record the flight information (Gonzalez *et al*., 2010). The forward velocity variations can be compensated by resampling the raw data in the azimuth direction. The trajectory deviations are commonly compensated by the so-called two-step motion compensation (MOCO) algorithms, which separate the aberration terms into range invariant and range variant components (Fornaro, 1999; Reigber *et al.*, 2006). First, the phase compensation of the middle range deviation term, usually referred to as the first-order MOCO, is carried out after the range compression step. Then, a phase compensation of the space variant deviation term, usually termed second-order MOCO, is accomplished after range cell migration (RCM) compensation and before the azimuth compression procedure (Marom *et al.*, 1990; Moreira and Huang, 1994; Fornaro *et al.*, 2006).

Two approximations are made in the two-step MOCO procedure. The first is the center-beam approximation, which assumes motion errors related to all targets within the azimuth beam to be equal to that at the center beam (Fornaro *et al.*, 2006). Therefore, the center-beam approximation will introduce azimuth-variant residual errors. The second is related to the topography variations, i.e., assuming that the illuminated surface is flat or that the reference DEM is accurate. When the differences between the actual elevation and the reference elevation are significant, the second approximation will enlarge the azimuth-variant residual errors caused by the center-beam approximation. The impacts of the residual motion compensation errors on the performance of single-antenna SAR imaging and on the interferometric phase of the cross-track interferometric SAR have been discussed in Marom *et al.* (1990), Fornaro *et al.* (2005; 2006), Reigber *et al.* (2006), and Li *et al.* (2014). For airborne ATI-SAR, since the fore- and aft-antennas are separated in the direction of the platform flight path, the trajectory deviations of the phase centers of each antenna are different at the same azimuth position due to the time interval. Thus, different residual uncompensated errors will be introduced to the fore- and aft-antenna and the interferometric phase will be influenced. Therefore, it is necessary to analyze the impacts of the residual uncompensated errors on the along-track interferometric phase, which has not been reported publicly until now.

To achieve higher radial velocity estimation accuracy, the interferometric phase must be accurate. The factors that influence the interferometric phase accuracy, including the imbalance between the two channels (Gierull, 2003), system noise (Zebker and Villasenor, 1992), and system imperfections (Madsen *et al.*, 1996; Dall *et al.*, 1997) (e.g., multi-path propagation and channel leakage), have been analyzed in Hirsch (2001) and Fischer *et al.* (2008). However, the influence of interferometric phase errors induced by the residual motion compensation errors during SAR imaging has not yet been considered for ATI-SAR. In this paper, we will discuss the phase errors induced by the residual motion compensation errors for airborne ATI-SAR and whether it can be neglected for different radial velocity accuracy requirements.

2 Principle of ATI-SAR and the procedure of MOCO

For simplicity, we consider the side-looking SAR without any squint angle. The ATI-SAR imaging geometry is shown in Fig. 1. We suppose that the ATI-SAR system is equipped with two antennas,

named fore-antenna (A_1) and aft-antenna (A_2), in the following sections. Also, the ATI 'Ping-Pong' mode is considered, in which the two antennas transmit and receive their own echoes alternately (Zhang, 2006). Fig. 1a is the ideal imaging geometry where the two antennas follow exactly the same trajectory, while Fig. 1b shows the perturbed geometry where the two antennas do not follow the same track because the aircraft position changes due to the atmospheric perturbation and strong winds. The coordinate system *xyz* in Fig. 1 is left-handed and centered at position *O*, or the 'nadir', which is the point on the Earth's surface directly below the fore-antenna at time t=0. The *x*-axis is parallel to the direction of the platform flight, the *z*-axis is directed vertically, and the *y*-axis is left-handed to the *x*- and *z*-axis.

In the ideal case (Fig. 1a), the two antennas of the ATI-SAR system are spatially separated by a fixed distance B_x along the flight direction. The two antennas illuminate the same scene at the same position

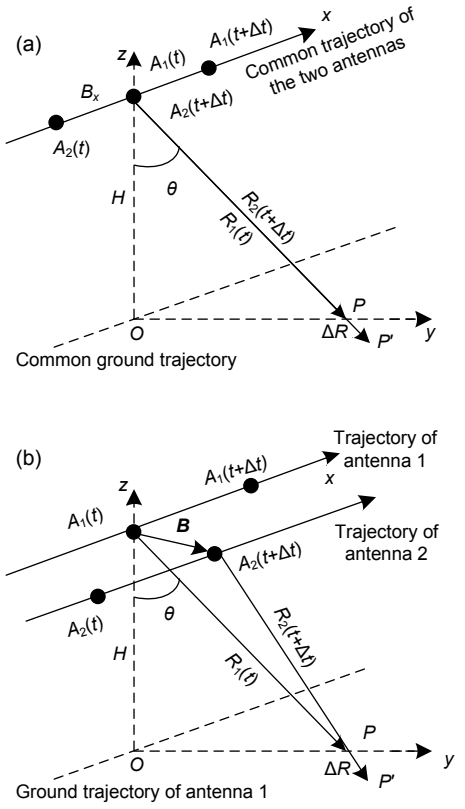

Fig. 1 ATI-SAR imaging geometry: (a) ideal geometry; (b) perturbed geometry

by a time interval $\Delta t=B_x/v_p$, where v_p is the constant platform velocity. During this time interval, the imaging geometry of the stationary targets remains the same, while the moving targets move a distance of $\Delta R=v_r\Delta t$ along the line-of-sight direction. Here, v_r is the radial velocity of the moving targets and is supposed to be constant during the short time interval. The interferogram of targets is formed by multiplying the image from the fore-antenna by the complex conjugate of the image from the aft-antenna. The interfeometric phase ϕ_{12} can be obtained by

$$\phi_{12}=\arg\{c_1(t)c_2^*(t+\Delta t)\}=\frac{4\pi}{\lambda}v_r\Delta t, \tag{1}$$

where λ is the wavelength of the radiation, $\arg\{\cdot\}$ returns the phase angle of a complex number, and $(\cdot)^*$ is the sign of complex conjugate. c_1 and c_2 are the complex images corresponding to the fore- and aft-antenna, respectively.

For the perturbed trajectory, where the baseline is $\boldsymbol{B}=(B_x, B_y, B_z)$ (Fig. 1b), the interferometric phase can be expressed as (Moccia and Rufino, 2001; Zhang and Hong, 2013)

$$\phi_{12}=\frac{4\pi}{\lambda}(-B_y\sin\theta+B_z\cos\theta+v_r\Delta t), \tag{2}$$

where B_y and B_z are the perpendicular baseline components in the direction of the cross-track and height, respectively.

Therefore, the range difference error δR between the two antennas can introduce an interferometric phase error $\delta\phi=4\pi\cdot\delta R/\lambda$. Moreover, the radial velocity error caused by the interferometric phase error, which can be deduced from the sensitivity of the radial velocity to the interferometric phase, can be written as $\delta v_r=\lambda\delta\phi/(4\pi\Delta t)$.

The ATI processing procedure includes imaging procedures and interferometric processing procedures. For airborne ATI-SAR systems, motion must be compensated to eliminate the trajectory deviations of the airplane. Fig. 2 illustrates the procedure of ATI-SAR processing with integrated MOCO. Raw data received by the two antennas are first processed separately and compressed into two single-look complex (SLC) images. During this procedure, the

two-step MOCO procedure is implemented and thus residual motion compensation errors occur for both channels due to center-beam approximation. The interferogram is acquired by multiplying the two interferometric images after azimuth time correction and image registration. At last, the radial velocities of moving targets are estimated from the interferometric phase.

Since the residual uncompensated errors caused by the center-beam approximation in MOCO procedures occur for both antennas, the differences of the residual motion compensation errors between the two antennas will result in interferometric phase errors, which further weakens the estimation accuracy of the radial velocity. In Sections 3 and 4, we will discuss the impact of residual motion compensation errors on the interferometric phase in the absence and presence of elevation errors, respectively.

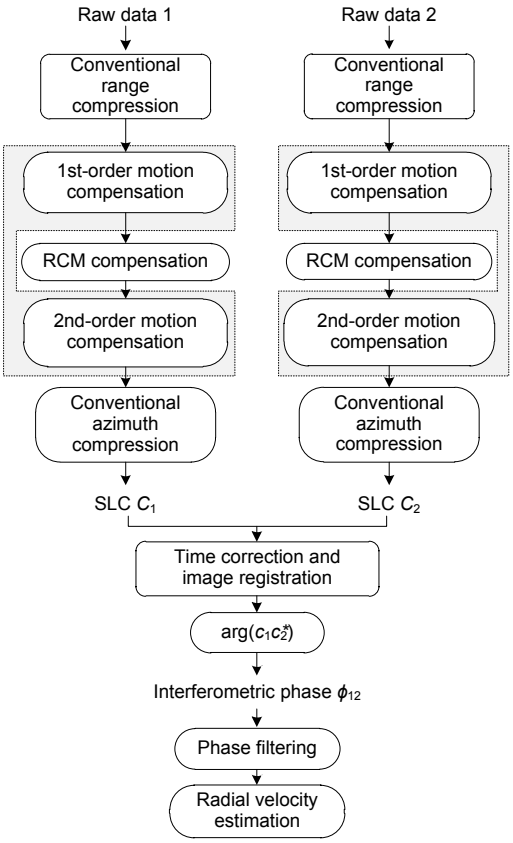

Fig. 2 Block diagram of SAR imaging with integrated MOCO and interferometric procedure for ATI-SAR
SLC: single-look complex image; RCM: range cell migration

3 Effects of residual uncompensated errors with accurate DEMs

Fig. 3 shows the imaging geometry with trajectory deviations but without elevation errors. For simplicity, we assume that the elevation of the scene is flat and equals that of the reference elevation (assumed to be zero). The coordinate system *xyz* in Fig. 3 is defined the same as in Fig. 1. In Fig. 3, A is the real position of the fore- or aft-antenna, A' is the nominal position of the antenna, and P is the position of the target.

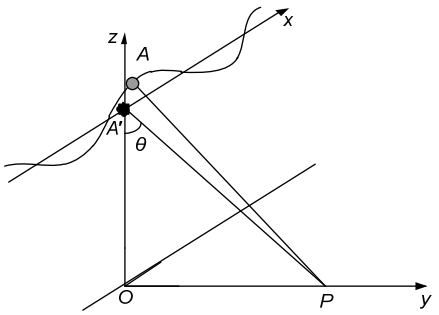

Fig. 3 Imaging geometry with trajectory deviations of airborne SAR without elevation errors

The analysis steps are listed as follows. First, the expressions of residual motion compensation errors are deduced for the fore-antenna and the aft-antenna (after a time interval Δt), respectively. Second, the difference between the uncompensated motion errors of the two antennas is obtained.

3.1 Residual uncompensated errors for the fore-antenna with accurate DEMs

For fore-antenna A_1, whose reference position is $(0, y_A, z_A)$ at zero azimuth time, the motion error at time t is assumed to be $[0, \Delta y(t), \Delta z(t)]$. The displacements $\Delta y(t)$ and $\Delta z(t)$ are extremely small compared with the slant range. The forward velocity of the platform is v_p and is assumed to be constant. Target P locates at (x_P, y_P, z_P) at t=0 with a constant velocity (v_x, v_y, v_z), and the azimuthal velocity v_x is assumed to be zero. The real motion error of P at time t, $\Delta R_{A_1P\_\mathrm{real}}(t)$, is expressed in Eq. (A1) in Appendix A. Under the center-beam assumption, the motion compensation error, $\Delta R_{A_1P\_\mathrm{COMO}}(t)$, is represented by Eq. (A2) in Appendix A.

Therefore, the residual MOCO errors for the moving targets under the illumination of the fore-antenna can be calculated from the subtraction of Eqs. (A1) and (A2), and is shown in Eq. (3), where R_0 is the distance between points A and P. Let v_y=v_z=0. Eq. (3) turns into Eq. (4), which is suitable for the stationary target. This result is consistent with that derived in Li *et al*. (2014).

3.2 Residual uncompensated errors for the aft-antenna with accurate DEMs

The aft-antenna moves to the same azimuth position of the fore-antenna after a short time interval Δt. Considering the perpendicular baseline components B_y and B_z, the reference position of the aft-antenna after time Δt is (0, y_A+B_y, z_A+B_z). The motion errors between the fore- and aft-antenna are different at the same azimuth position because of the time interval. The motion errors of the aft-antenna [0, $\Delta y(t+\Delta t)$, $\Delta z(t+\Delta t)$] can be assumed to be the sum of [0, $\Delta y(t)$, $\Delta z(t)$] and [0, $\delta y(t)$, $\delta z(t)$], where $\delta y(t)$ and $\delta z(t)$ are the differences of the motion errors between the two antennas in the y and z directions, respectively. At the same time, the moving target P moves to (x_P, y_P+$v_y\Delta t$, z_P+$v_z\Delta t$) after the time interval. The real motion error of the moving target P during the illumination of the aft-antenna, $\Delta R_{A_2D\_\mathrm{real}}(t+\Delta t)$, is shown in Eq. (A3). Under the center-beam assumption, the motion compensation error, $\Delta R_{A_2D\_\mathrm{COMO}}(t+\Delta t)$, is shown in Eq. (A4). Therefore, the residual error after MOCO is obtained and expressed in Eq. (5).

3.3 Interferometric phase errors

The difference of the residual MOCO errors between the fore- and aft-antenna are shown in Eq. (6), which are obtained by subtracting Eq. (3) from Eq. (5). In Eq. (6), sin θ=(y_P−y_A)/R_0 and cos θ=(z_A−z_P)/R_0.

We can conclude that the interferometric phase errors caused by the residual uncompensated errors with accurate DEMs are extraordinarily small since the residual uncompensated errors in Eq. (6) are very small during the whole synthetic aperture time.

$$\begin{aligned}\Delta R_{A_1P\_\mathrm{res}}(t) &= \Delta R_{A_1P\_\mathrm{real}}(t) - \Delta R_{A_1P\_\mathrm{COMO}}(t)\\ &\approx -\frac{\Delta y(t)\cdot v_y t + \Delta z(t)\cdot v_z t}{R_0}\\ &\quad + \frac{(y_A-y_P)^2\Delta y(t)\cdot v_y t + (z_A-z_P)^2\Delta z(t)\cdot v_z t + (y_A-y_P)(z_A-z_P)(\Delta y(t)\cdot v_z t + \Delta z(t)\cdot v_y t)}{R_0^3}\\ &\quad - \frac{(v_{\mathrm{p}}t-x_P)^2[(y_A-y_P)\Delta y(t)+(z_A-z_P)\Delta z(t)]}{2R_0^3}.\end{aligned} \tag{3}$$

$$\Delta R_{A_1P\_\mathrm{res}}(t) = -\frac{(v_{\mathrm{p}}t-x_P)^2[(y_A-y_P)\Delta y(t)+(z_A-z_P)\Delta z(t)]}{2R_0^3}. \tag{4}$$

$$\begin{aligned}\Delta R_{A_2P\_\mathrm{res}}(t+\Delta t) &= \Delta R_{A_2P\_\mathrm{real}}(t+\Delta t) - \Delta R_{A_2P\_\mathrm{COMO}}(t+\Delta t)\\ &\approx -\frac{[\Delta y(t)+\delta y(t)]\cdot(v_y\Delta t+v_y t)+[\Delta z(t)+\delta z(t)]\cdot(v_z\Delta t+v_z t)}{R_0}\\ &\quad + \frac{(y_A-y_P)^2[\Delta y(t)+\delta y(t)](v_y\Delta t+v_y t)+(z_A-z_P)^2[\Delta z(t)+\delta z(t)](v_z\Delta t+v_z t)}{R_0^3}\\ &\quad + \frac{(y_A-y_P)(z_A-z_P)\{[\Delta y(t)+\delta y(t)](v_z\Delta t+v_z t)+[\Delta z(t)+\delta z(t)](v_y\Delta t+v_y t)\}}{R_0^3}\\ &\quad - \frac{(v_{\mathrm{p}}t-x_P)^2\{(y_A-y_P)[\Delta y(t)+\delta y(t)]+(z_A-z_P)[\Delta z(t)+\delta z(t)]\}}{2R_0^3}.\end{aligned} \tag{5}$$

$$\begin{aligned}\delta R(t) &= \Delta R_{A_2P\_\mathrm{res}}(t+\Delta t) - \Delta R_{A_1P\_\mathrm{res}}(t)\\ &\approx -\frac{\Delta y(t)\cdot v_y\Delta t + \Delta z(t)\cdot v_z\Delta t + \delta y(t)\cdot(v_y\Delta t + v_y t) + \delta z(t)\cdot(v_z\Delta t + v_z t)}{R_0}\\ &\quad + \frac{\sin^2\theta[\Delta y(t)\cdot v_y\Delta t + \delta y(t)\cdot(v_y\Delta t + v_y t)] + \cos^2\theta[\Delta z(t)\cdot v_z\Delta t + \delta z(t)\cdot(v_z\Delta t + v_z t)]}{R_0}\\ &\quad - \frac{\sin\theta\cos\theta\{[\Delta y(t)+\delta y(t)]\cdot v_z\Delta t + [\Delta z(t)+\delta z(t)]\cdot v_y\Delta t + v_y t\cdot\delta z(t) + v_z t\cdot\delta y(t)\}}{R_0}\\ &\quad + \frac{(v_\mathrm{p}t - x_P)^2[\sin\theta\delta y(t) - \cos\theta\delta z(t)]}{2R_0^2}.\end{aligned} \tag{6}$$

4 Effects of residual uncompensated errors with inaccurate DEMs

If the elevation of the scene is unknown or different from the reference elevation, and if we still use the reference elevation to compensate for the motion errors, then the residual uncompensated errors will be enlarged. Fig. 4 shows the imaging geometry with trajectory deviations and the presence of elevation errors. The height of target D is h compared with the reference terrain.

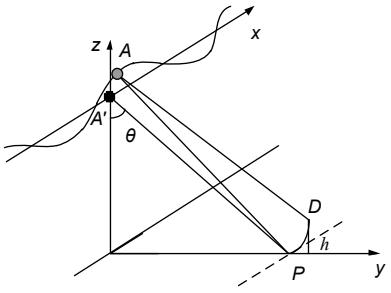

Fig. 4 Imaging geometry with trajectory deviations in the presence of elevation errors

4.1 Residual uncompensated errors for the fore-antenna with inaccurate DEMs

Similar to the supposition in Section 3.1, the fore-antenna is located at $(0, y_A, z_A)$ at zero azimuth time, and the motion error is $[0, \Delta y(t), \Delta z(t)]$ at time t. Suppose that the position of target D is $(0, y_D, z_D)$ at zero time and that its relative height to the reference elevation is h. The target moves with a constant velocity $(0, v_y, v_z)$. In practice, the relative height of target D is unknown, and we use point P in the reference plane, which satisfies the condition $|A_1D|=|A_1P|$, to replace target D in the MOCO procedure. Suppose the position of P is $(0, y_P, z_P)$ and $z_D=z_P+h$. Let $y_D=y_P+y_\varepsilon$, and y_ε can be calculated from $|A_1D|=|A_1P|$. The real motion error of D, $\Delta R_{A_1D\_\mathrm{real}}(t)$, is expressed in Eq. (B1) in Appendix B.

Under the center-beam assumption, the motion compensation error of target D can be obtained by the motion compensation error of target P, that is, $\Delta R_{A_1D\_\mathrm{COMO}}(t)=\Delta R_{A_1P\_\mathrm{COMO}}(t)$. Therefore, the residual uncompensated motion error of target D can be calculated using Eq. (7), which is given in the next page.

4.2 Residual uncompensated errors for the aft-antenna with inaccurate DEMs

For the aft-antenna, which is separated from the fore-antenna by the baseline vector $\boldsymbol{B}=(B_x, B_y, B_z)$, the reference position is $(0, y_A+B_y, z_A+B_z)$ after a time interval Δt. The trajectory error of the aft-antenna can be written as $[0, \Delta y(t), \Delta z(t)]+[0, \delta y(t), \delta z(t)]$, which is the same as that in Section 3.2. Target D moves to the position of $(x_D, y_D+v_y\Delta t, z_D+v_z\Delta t)$ after the time interval. The height and velocity information of D is unknown and point Q in the reference plane which satisfies $|A_2D|=|A_2Q|$ is used to replace the moving target D during the MOCO procedure. The position of Q is written as (x_Q, y_Q, z_Q), where $x_D=x_Q$ and $z_D=z_Q+h$. Suppose that $y_D = y_Q + y'_\varepsilon$, and y'_ε can be calculated by $|A_2D|=|A_2Q|$. The real motion error of target D, $\Delta R_{A_2D\_\mathrm{real}}(t)$, is expressed in Eq. (B2) in Appendix B.

Under the center-beam assumption, the motion compensation errors of target D, $\Delta R_{A_2D\_\mathrm{COMO}}(t)$, can be obtained based on the motion compensation error of target Q, which is shown in Eq. (B3).

Therefore, the residual uncompensated error is derived and shown in Eq. (8), where the second term is equal to that of Eq. (5) except that (y_P, z_P) is

replaced by (y_Q, z_Q). Here z_P=z_Q, but y_P≠y_Q. The first term is the range error caused by the elevation errors, as is shown in Eq. (9).

4.3 Interferometric phase errors

From the above analysis, the residual uncompensated motion errors can be obtained by Eq. (10). Obviously, the residual uncompensated errors will be enlarged when the elevation errors exist. By comparing Eq. (10) with Eq. (6), we can see that the residual uncompensated errors are related with the elevation error h and the flight stability $\delta y(t)$ and $\delta z(t)$. When the elevation error h or the differences of the trajectory deviations between the two antennas are significant, the residual uncompensated motion errors may not be neglected. The simulation results in the next section will demonstrate this idea.

4.4 Impact of trajectory measurement errors

In the above analysis, the measurement errors of the trajectory measurement equipment, such as the GPS systems, are included in the trajectory errors. If we consider the GPS measurement errors separately, the trajectory deviations of the for-antenna should be written as [0, $\Delta y(t)+\sigma_y(t)$, $\Delta z(t)+\sigma_z(t)$] instead of [0, $\Delta y(t)$, $\Delta z(t)$], where $\sigma_y(t)$ and $\sigma_z(t)$ represent the GPS system errors in y and z directions, respectively. Similarly, the trajectory deviations of the aft-antenna are [0, $\Delta y(t+\Delta t)+\sigma_y(t+\Delta t)$, $\Delta z(t+\Delta t)+\sigma_z(t+\Delta t)$] instead of [0, $\Delta y(t+\Delta t)$, $\Delta z(t+\Delta t)$]. Suppose the GPS system errors in the time interval Δt are $\xi_y(t)$ and $\xi_z(t)$ in the y and z directions respectively. The trajectory deviations of the aft-antenna can be expressed by Eq. (11).

$$\begin{aligned}\Delta R_{A_1D\_\mathrm{res}}(t) \approx & -\frac{\Delta y(t)\cdot v_y t+\Delta z(t)\cdot v_z t}{R_0}\\ & +\frac{(y_A-y_P)^2\Delta y(t)\cdot v_y t+(z_A-z_P)^2\Delta z(t)\cdot v_z t+(y_A-y_P)(z_A-z_P)[\Delta y(t)\cdot v_z t+\Delta z(t)\cdot v_y t]}{R_0^3}\\ & -\frac{(v_{\mathrm{p}}t-x_P)^2[(y_A-y_P)\Delta y(t)+(z_A-z_P)\Delta z(t)]}{2R_0^3}+\frac{h}{y_A-y_P}\left[\frac{z_A-z_P}{R_0}\Delta y(t)-\frac{y_A-y_P}{R_0}\Delta z(t)\right].\end{aligned} \tag{7}$$

$$\begin{aligned}\Delta R_{A_2D\_\mathrm{res}}(t+\Delta t) &= \Delta R_{A_2D\_\mathrm{real}}(t+\Delta t)-\Delta R_{A_2D\_\mathrm{COMO}}(t+\Delta t)\\ &= \Delta R_{A_2D\_\mathrm{real}}(t+\Delta t)-\Delta R_{A_2Q\_\mathrm{real}}(t+\Delta t)+\Delta R_{A_2Q\_\mathrm{real}}(t+\Delta t)-\Delta R_{A_2Q\_\mathrm{COMO}}(t+\Delta t)\\ &= \Delta R_{QD2}(t+\Delta t)+\Delta R_{A_2Q\_\mathrm{res}}(t+\Delta t).\end{aligned} \tag{8}$$

$$\begin{aligned}\Delta R_{QD2}(t+\Delta t) &\approx -\frac{\Delta y(t+\Delta t)\cdot y'_{\varepsilon}+\Delta z(t+\Delta t)\cdot h}{R_0}\\ &\approx \frac{h}{y_A+B_y-y_D}\left\{\frac{z_A+B_z-z_P}{R_0}[\Delta y(t)+\delta y(t)]-\frac{y_A+B_y-y_D}{R_0}[\Delta z(t)+\delta z(t)]\right\}.\end{aligned} \tag{9}$$

$$\begin{aligned}\delta R(t) &= \Delta R_{A_2D\_\mathrm{res}}(t+\Delta t)-\Delta R_{A_1D\_\mathrm{res}}(t)\\ &\approx \frac{h[\cos\theta\delta y(t)+\sin\theta\delta z(t)]}{y_A-y_P}-\frac{\Delta y(t)\cdot v_y\Delta t+\Delta z(t)\cdot v_z\Delta t+\delta y(t)\cdot(v_y\Delta t+v_y t)+\delta z(t)\cdot(v_z\Delta t+v_z t)}{R_0}\\ &\quad+\frac{\sin^2\theta[\Delta y(t)\cdot v_y\Delta t+\delta y(t)\cdot(v_y\Delta t+v_y t)]+\cos^2\theta[\Delta z(t)\cdot v_z\Delta t+\delta z(t)\cdot(v_z\Delta t+v_z t)]}{R_0}\\ &\quad-\frac{\sin\theta\cos\theta\{[\Delta y(t)+\delta y(t)]\cdot v_z\Delta t+[\Delta z(t)+\delta z(t)]\cdot v_y\Delta t+v_y t\cdot\delta z(t)+v_z t\cdot\delta y(t)\}}{R_0}\\ &\quad+\frac{(v_{\mathrm{p}}t-x_P)^2}{2R_0^2}[\sin\theta\delta y(t)-\cos\theta\delta z(t)].\end{aligned} \tag{10}$$

$$\begin{aligned}&[0,\Delta y(t+\Delta t)+\sigma_y(t+\Delta t),\Delta z(t+\Delta t)+\sigma_z(t+\Delta t)]\\&=[0,\Delta y(t)+\sigma_y(t),\Delta z(t)+\sigma_z(t)]\\&\quad+[0,\delta y(t)+\xi_y(t),\delta z(t)+\xi_z(t)].\end{aligned}\tag{11}$$

Under these circumstances, the additional residual uncompensated motion errors between the two antennas caused by the GPS system errors can be written as Eq. (10), except that $\Delta y(t)$ should be replaced by $\sigma_y(t)$, $\Delta z(t)$ be replaced by $\sigma_z(t)$, $\delta y(t)$ be replaced by $\xi_y(t)$, and $\delta z(t)$ be replaced by $\xi_z(t)$.

The variations of the GPS measurement errors ($\xi_y(t)$ and $\xi_z(t)$) within the time interval Δt are very small compared with $\delta y(t)$ and $\delta z(t)$. Moreover, the GPS measurement errors $\sigma_y(t)$ and $\sigma_z(t)$ (about several centimeters) are relatively small compared with the antenna trajectory deviations $\Delta y(t)$ and $\Delta z(t)$ (depending on the flight condition, about several meters or tens of meters). Therefore, the uncompensated moving errors caused by the GPS measurement error are relatively small compared with the result of Eq. (10) and can be neglected.

5 Simulation and demonstration

In this section, we use the airborne ATI-SAR system parameters to simulate the impacts of residual uncompensated motion errors on the interferometric phase and the radial velocity estimation accuracy of ATI-SAR discussed in Sections 3 and 4.

5.1 Verification of the derivations

The correctness of the derived formulas in Sections 3 and 4 is verified by the simulated airborne parameters listed in Table 1. The three baseline components of the real system are B_x=0.996 m, B_y=0.087 m, and B_z=0.035 m, which can be easily achieved from the baseline length and the attitude of the platform (Cumming and Wong, 2004; Zhang and Hong, 2013).

The simulation results are shown in Fig. 5. The velocity of the moving target is selected to be (0, 0.5, 0) m/s, which corresponds to a radial velocity of 0.35 m/s and is smaller than the maximum unambiguous ATI velocity. Figs. 5a–5b are the results for the absence of DEM. Fig. 5a shows the theoretically derived residual range errors (Eq. (6)) and the simulated residual range errors during the synthetic aperture time. Fig. 5b shows the differences between the theoretical and simulated residual range errors. Figs. 5c–5d show the corresponding results with the DEM errors present. We can conclude that the derived residual range errors are consistent with that of the simulation results, and therefore the correctness of the derived formulas is verified.

Table 1 Airborne simulation parameters

Parameter	Value	Parameter	Value
Wave length (cm)	3.125	Baseline length (m)	1
Flight height (m)	3000	Squint angle (degree)	0
Flight velocity (m/s)	150	Look-angle (degree)	45
Antenna length (m)	2	Yaw angle (degree)	5
ATI time interval (ms)	6.7	Pitch angle (degree)	2

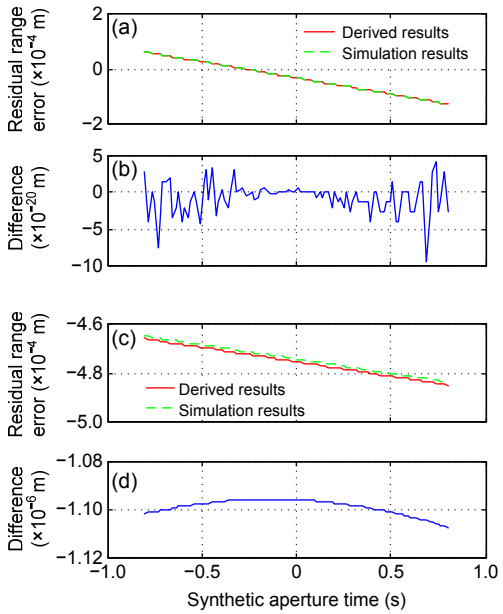

Fig. 5 Correctness of the derived residual range errors: (a) theoretical and simulated residual range errors and (b) the differences between theoretical and simulated residual range errors in the absence of DEM errors; (c) theoretical and simulated residual range errors and (d) the differences between theoretical and simulated residual range errors in the presence of DEM errors

After verifying the correctness of the theoretical derivations, we simulate 30 moving targets with different velocities for further validation. The trajectory deviations are introduced and different elevation errors are considered in the simulations. Other error sources, e.g., phase imbalance, differential channel

delay between the two interferometric channels, and the indetermination of the baseline length, are neglected. The simulation method is described as follows: First, raw data with trajectory deviations of 30 moving targets with different velocities are simulated for the two antennas. Then, procedures including MOCO, range Doppler imaging, and interferometric processing as shown in Fig. 2, are conducted. Finally, the radial velocities of the moving targets are estimated from the interferometric phase. The velocity errors deduced by the interferometric phase errors caused by residual MOCO errors as shown in Eqs. (6) and (10) are also obtained. By comparing the velocity errors obtained from the simulation results and the theoretical derivations, we can verify the analysis of the effects of residual uncompensated motion errors.

In the simulations, the trajectory deviations are supposed to be 3 m, and the velocities of the 30 targets are varying linearly from 0.2 m/s to 0.71 m/s, which are smaller than the maximum unambiguous ATI velocities. The elevations of the targets are supposed to be zero and different reference elevations are used in the MOCO procedures to simulate different DEM errors (Note that the DEM errors here actually include the height of the moving target above the ground and the elevation errors between the actual topography and the reference topography). Here, we assume the DEM error is 10 m. Fig. 6 illustrates the results of the simulated radial velocity estimation errors and the theoretically deduced radial velocity estimation errors.

Figs. 6a–6c are the simulation results in the absence of DEM errors. Fig. 6a shows the theoretically derived radial velocity estimation errors, Fig. 6b shows the simulated radial velocity estimation errors, and Fig. 6c shows the differences between the theoretical and simulation results in the absence of DEM errors. We can conclude that the simulation results are consistent with the theoretical results. Figs. 6d–6f show the corresponding results with a DEM error of 10 m.

Comparing Figs. 6a–6c and Figs. 6d–6f, we can find that the velocity errors caused by the uncompensated motion errors in the presence of DEM errors are much larger than those with accurate DEM. That is to say, DEM errors will enlarge the impacts of uncompensated motion errors.

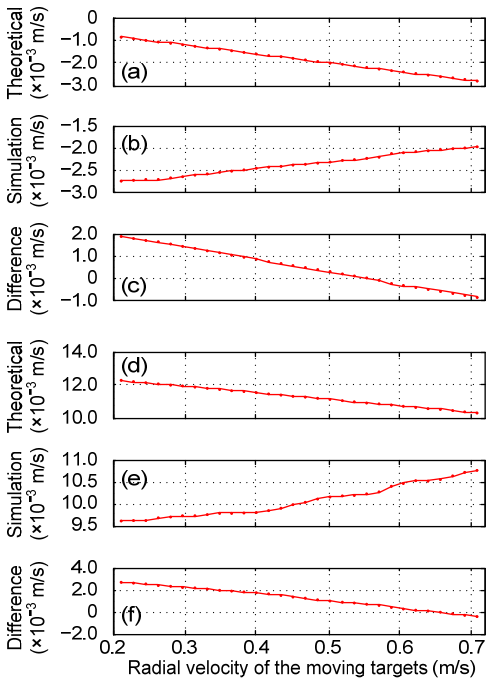

Fig. 6 Radial velocity estimation error simulation for 30 moving targets with different velocities: (a)–(c) theoretical, simulation, and the differences between the theoretical and simulated estimation errors, in the absence of DEM errors; (d)–(f) theoretical, simulation, and the differences between the theoretical and simulated estimation errors, in the presence of DEM errors

5.2 Effects of uncompensated motion errors

The effects of uncompensated motion errors on radial velocity estimation accuracies under different elevation errors and different look angles are discussed in this section. A set of real flight data recorded by navigation systems such as GPS or POS (Position and Orientation System) in an airborne flight experiment are used to obtain the motion errors of the two antennas. Figs. 7a and 7b show the flight path in the direction of cross-track and height, respectively. Figs. 7c and Fig. 7d show the differences of the trajectories between the two antennas in the time interval Δt. The maximum values of $\delta y(t)$ and $\delta z(t)$ in the ATI temporal baseline (time interval) are 0.006 m and 0.003 m, respectively.

From the analysis in Section 5.1, we can see that with accurate DEM, the impacts of uncompensated motion errors can be neglected for most applications. In the presence of elevation errors, however, the interferometric phase errors caused by the differences between the motion compensation errors of the two

antennas are greatly enlarged. Fig. 8 illustrates the radial velocity estimation errors corresponding to different elevation errors and different look-angles. The velocity of the moving target is still set to (0, 0.5, 0) m/s.

For example, when the look-angle is 45°, the effects of residual uncompensated motion errors on the interferometric phase could not be neglected if the elevation errors are larger than 25 m for the radial velocity estimation accuracy of 0.01 m/s. Moreover, the flight stability affects the interferometric phase errors caused by the differences of the residual uncompensated errors between the two ATI antennas. Therefore, the impacts of uncompensated motion errors on the performance of airborne ATI-SAR must be considered if DEM errors are significant.

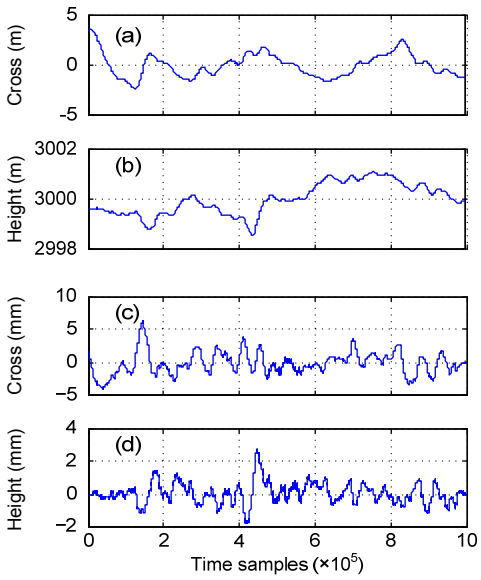

Fig. 7 The flight path in the directions of cross-track (a) and height (b) and the differences of the trajectories between the two antennas in the time interval Δt in the directions of cross-track (c) and height (d)

6 Conclusions

We addressed the residual uncompensated motion errors in airborne ATI-SAR MOCO. It is shown that the center-beam approximation and referenced DEM assumption introduce phase errors during MOCO procedures for each ATI antenna. The differences of the residual uncompensated motion errors between the two ATI antennas may lead to ATI interferometric phase errors, which further affect the radial velocity estimation accuracy. It has been proved that the interferometric phase errors caused by the residual uncompensated motion errors under center-beam approximation in the MOCO procedure can be neglected when the reference elevation of the scene is accurate or approximately accurate. However, for the cases of unknown or significantly inaccurate DEM, the effects of the residual uncompensated motion errors on the interferometric phase depend greatly on the elevation accuracy and the flight stability. Airborne simulation parameters are used to verify the correctness of the analysis. Moreover, the quantitative relationship between radial velocity errors and DEM errors is given and the critical value of the DEM error when the uncompensated motion errors cannot be neglected is illustrated. The study provides a theoretical basis for practical applications and is instructive for repeat-pass ATI-SAR.

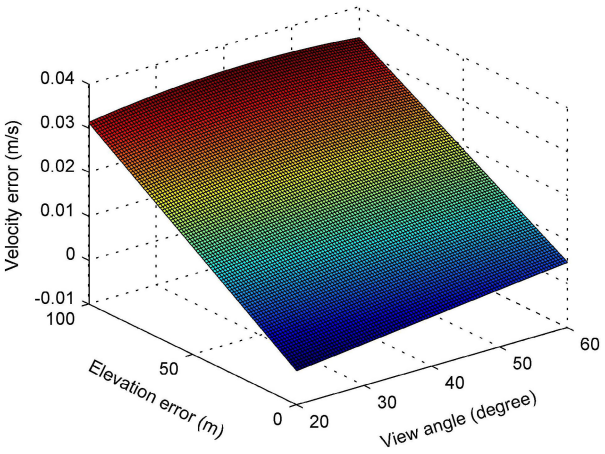

Fig. 8 Radial velocity estimation errors corresponding to different elevation errors and different view angles

Acknowledgements

The authors would like to thank the anonymous reviewers for their precious time and valuable suggestions that are very helpful for improving the paper and our future research.

References

Budillon, A., Pascazio, V., Schirinzi, G., 2008. Estimation of radial velocity of moving targets by along-track interferometric SAR systems. *IEEE Geosci. Remote Sens. Lett.*, **5**(3):349-353. http://dx.doi.org/10.1109/lgrs.2008.915937

Chapin, E., Chen, C.W., 2009. Airborne along-track interferometry for GMTI. *IEEE Aerosp. Electron. Syst. Mag.*, **24**(5):13-18. http://dx.doi.org/10.1109/maes.2009.5109948

Chen, C.W., 2004. Performance assessment of along-track interferometry for detecting ground moving targets. Proc. IEEE Radar Conf., 99-104. http://dx.doi.org/10.1109/nrc.2004.1316403

Cumming, I.G., Wong, F.H., 2004. Digital Processing of Synthetic Aperture Radar Data: Algorithms and Implementation. Artech House, London.

Dall, J., Grinder-Pedersen, J., Madsen, S.N., 1997. Calibration of a high resolution airborne 3D SAR. IEEE Int. Geoscience and Remote Sensing Symp., p.1018-1021. http://dx.doi.org/10.1109/igarss.1997.615329

Fischer, J., Baumgartner, S., Reigber, A., *et al.*, 2008. Geometric, radiometric, polarimetric and along-track interferometric calibration of the new F-SAR system of DLR in X-Band. 7th European Conf. on Synthetic Aperture Radar, p.109-112.

Fornaro, G., 1999. Trajectory deviations in airborne SAR: analysis and compensatin. *IEEE Trans. Aerosp. Electron. Syst.*, **35**(3):997-1009. http://dx.doi.org/10.1109/7.784069

Fornaro, G., Franceschetti, G., Perna, S., 2005. Motion compemsatiom errors: effects on the accuracy of airborne SAR images. *IEEE Trans. Aerosp. Electr. Syst.*, **41**(4): 1338-1352. http://dx.doi.org/10.1109/taes.2005.1561888

Fornaro, G., Franceschetti, G., Perna, S., 2006. On center-beam approximation in SAR motion compensation. *IEEE Geosci. Remote Sens. Lett.*, **3**(2):276-280. http://dx.doi.org/10.1109/lgrs.2005.863391

Gierull, C.H., 2003. Digital Channel Balancing of Along-Track Interferometric SAR Data. Technical Memorandum No. DRDC-OTTAWA-TM-2003-024, Defence R&D Canada-Ottawa.

Glerull, C.H., 2002. Moving Target Detection with Along-Track SAR Interferometry: a Theoretical Analysis. Technical Memorandum No. DRDC-OTTAWA-TR-2002-084, Defence R&D Canada-Ottawa.

Goldstein, R.M., Zebker, H.A., 1987. Interferometric radar measurement of ocean surface currents. *Nature*, **328**(6132):707-709. http://dx.doi.org/10.1038/328707a0

Gonzalez, J.H., Bachmann, M., Krieger, G., *et al.*, 2010. Development of the TanDEM-X calibration concept: analysis of systematic errors. *IEEE Trans. Geosci. Remote Sens.*, **48**(2):716-726. http://dx.doi.org/10.1109/tgrs.2009.2034980

Hirsch, O., 2001. Calibration of an airborne along-track interferometric SAR system for accurate measurement of velocities. IEEE Int. Geoscience and Remote Sensing Symp., p.558-560. http://dx.doi.org/10.1109/igarss.2001.976221

Imel, D.A., 2002. AIRSAR along-track interferometry data. AIRSAR Earth Science and Applications Workshop, p.1-58.

Li, F.F., Qiu, X.L., Meng, D.D., *et al.*, 2014. Effects of motion compensation errors on performance of airborne dual-antenna InSAR. *J. Electr. Inform. Technol.*, **35**(3): 559-567 (in Chinese). http://dx.doi.org/10.3724/sp.j.1146.2012.00850

Madsen, S.N., Skou, N., Woelders, K., *et al.*, 1996. EMISAR single pass topographic SAR interferometer modes. IEEE Geoscience and Remote Sensing Symp., p.674-676. http://dx.doi.org/10.1109/igarss.1996.516439

Marom, M., Goldstein, R.M., Thornton, E.B., *et al.*, 1990. Remote sensing of ocean wave spectra by interferometric synthetic aperture radar. *Nature*, **345**(6278):793-795. http://dx.doi.org/10.1038/345793a0

Moccia, A., Rufino, G., 2001. Spaceborne along-track SAR interferometry: performance analysis and mission scenarios. *IEEE Trans. Aerosp. Electron. Syst.*, **37**(1): 199-213. http://dx.doi.org/10.1109/7.913679

Moreira, A., Huang, Y.H., 1994. Airborne SAR processing of highly squinted data using a chirp scaling approach with integrated motion compensation. *IEEE Trans. Geosci. Remote Sens.*, **32**(5):1029-1040. http://dx.doi.org/10.1109/36.312891

Raney, R.K., 1971. Synthetic aperture imaging radar and moving targets. *IEEE Trans. Aerosp. Electron. Syst.*, **AES-7**(3):499-505. http://dx.doi.org/10.1109/taes.1971.310292

Reigber, A., Alivizatos, E., Potsis, A., *et al.*, 2006. Extended wavenumber-domain synthetic aperture radar focusing with integrated motion compensation. *IEE Proc.-Radar Sonar Navig.*, **153**(3):301-310. http://dx.doi.org/10.1049/ip-rsn:20045087

Rosen, P.A., Hensley, S., Joughin, I.R., *et al.*, 2000. Synthetic aperture radar interferometry. *Proc. IEEE*, **88**(3):333-382. http://dx.doi.org/10.1109/5.838084

Zebker, H.A., Villasenor, J., 1992. Decorrelation in interferometric radar echoes. *IEEE Trans. Geosci. Remote Sens.*, **30**(5):950-959. http://dx.doi.org/10.1109/36.175330

Zhang, H., Hong, J., 2013. Sensitivity analysis of along-track interferometric synthetic aperture radar (ATI-SAR) in the presence of squint. IET Int. Radar Conf., p.1-5. http://dx.doi.org/10.1049/cp.2013.0181

Zhang, Y.H., 2006. Along Track Interferometry Synthetic Aperture Radar Techniques for Ground Moving Target Detection. Technical Report No. AFRL-SN-RS-TR-2005-410, Stiefvater Consultants.

Zink, M., Krieger, G., Fiedler, H., *et al.*, 2007. The TanDEM-X mission: overview and status. IEEE Int. Geoscience and Remote Sensing Symp., p.3944-3947. http://dx.doi.org/10.1109/igarss.2007.4423711

Appendix A: Equations for deriving interferometric phase errors with accurate DEMs

According to Fig. 3, the real motion error of point P during the illumination of the fore-antenna at time t can be expressed by

$$\begin{aligned}\Delta R_{A_1P\_\text{real}}(t)=&\sqrt{(v_\text{p}t-x_P)^2+(y_A+\Delta y(t)-y_P-v_yt)^2+(z_A+\Delta z(t)-z_P-v_zt)^2}\\&-\sqrt{(v_\text{p}t-x_P)^2+(y_A-y_P-v_yt)^2+(z_A-z_P-v_zt)^2}.\end{aligned}\tag{A1}$$

Under the center-beam assumption, the motion compensation error of point P is

$$\Delta R_{A_1P\_\text{COMO}}(t)=\sqrt{(y_A+\Delta y(t)-y_P)^2+(z_A+\Delta z(t)-z_P)^2}-\sqrt{(y_A-y_P)^2+(z_A-z_P)^2}.\tag{A2}$$

The real motion error of moving target P during the illumination of the aft-antenna is

$$\begin{aligned}&\Delta R_{A_2P\_\text{real}}(t+\Delta t)\\&=\sqrt{(v_\text{p}t-x_P)^2+(y_A+B_y+\Delta y(t+\Delta t)-y_P-v_y\Delta t-v_yt)^2+(z_A+B_z+\Delta z(t+\Delta t)-z_P-v_z\Delta t-v_zt)^2}\\&\quad-\sqrt{(v_\text{p}t-x_P)^2+(y_A+B_y-y_P-v_y\Delta t-v_yt)^2+(z_A+B_z-z_P-v_z\Delta t-v_zt)^2}.\end{aligned}\tag{A3}$$

The motion compensation error of target P during the illumination of the aft-antenna under the center-beam assumption is

$$\Delta R_{A_2P\_\text{COMO}}(t+\Delta t)=\sqrt{(y_A+B_y+\Delta y(t+\Delta t)-y_P)^2+(z_A+B_z+\Delta z(t+\Delta t)-z_P)^2}-\sqrt{(y_A+B_y-y_P)^2+(z_A+B_z-z_P)^2}.\tag{A4}$$

Appendix B: Equations for deriving interferometric phase errors with inaccurate DEMs

According to Fig. 4, the real motion error of D during the illumination of the fore-antenna is

$$\begin{aligned}\Delta R_{A_1D\_\text{real}}(t)=&\sqrt{(v_\text{p}t-x_D)^2+(y_A+\Delta y(t)-y_D-v_yt)^2+(z_A+\Delta z(t)-z_D-v_zt)^2}\\&-\sqrt{(v_\text{p}t-x_D)^2+(y_A-y_D-v_yt)^2+(z_A-z_D-v_zt)^2}.\end{aligned}\tag{B1}$$

The real motion error of D during the illumination of the aft-antenna is

$$\begin{aligned}&\Delta R_{A_2D\_\text{real}}(t+\Delta t)\\&=\sqrt{(v_\text{p}t-x_D)^2+(y_A+B_y+\Delta y(t)+\delta y(t)-y_D-v_y\Delta t-v_yt)^2+(z_A+B_z+\Delta z(t)+\delta z(t)-z_D-v_z\Delta t-v_zt)^2}\\&\quad-\sqrt{(v_\text{p}t-x_D)^2+(y_A+B_y-y_D-v_y\Delta t-v_yt)^2+(z_A+B_z-z_D-v_z\Delta t-v_zt)^2}.\end{aligned}\tag{B2}$$

Under the center-beam assumption, the motion compensation errors of target D can be obtained by the motion compensation error of target Q:

$$\begin{aligned}&\Delta R_{A_2D\_\text{COMO}}(t+\Delta t)=\Delta R_{A_2Q\_\text{COMO}}(t+\Delta t)\\&=\sqrt{(y_A+B_y+\Delta y(t)+\delta y(t)-y_Q)^2+(z_A+B_z+\Delta z(t)+\delta z(t)-z_Q)^2}-\sqrt{(y_A+B_y-y_Q)^2+(z_A+B_z-z_Q)^2}.\end{aligned}\tag{B3}$$